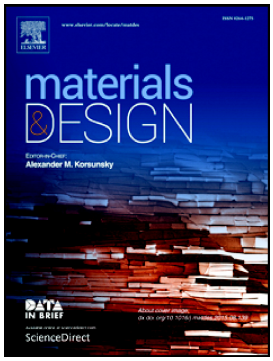

Continuous nanobelts of nickel oxide–cobalt oxide hybrid with improved capacitive charge storage properties

Midhun Harilal, Syam G. Krishnan, Bincy Lathakumary Vijayan, M. Venkatashamy Reddy, Stefan Adams, Andrew R. Barron, Mashitah M. Yusoff, Rajan Jose

PII: S0264-1275(17)30263-0
DOI: doi: 10.1016/j.matdes.2017.03.024
Reference: JMADE 2858

To appear in: *Materials & Design*

Received date: 30 January 2017
Revised date: 6 March 2017
Accepted date: 7 March 2017

Please cite this article as: Midhun Harilal, Syam G. Krishnan, Bincy Lathakumary Vijayan, M. Venkatashamy Reddy, Stefan Adams, Andrew R. Barron, Mashitah M. Yusoff, Rajan Jose , Continuous nanobelts of nickel oxide–cobalt oxide hybrid with improved capacitive charge storage properties. The address for the corresponding author was captured as affiliation for all authors. Please check if appropriate. Jmade(2017), doi: 10.1016/j.matdes.2017.03.024

Continuous nanobelts of nickel oxide–cobalt oxide hybrid with improved capacitive charge storage properties

Midhun Harilal,[1] Syam G. Krishnan,[1] Bincy Lathakumary Vijayan,[1] M. Venkatashamy Reddy,[2] Stefan Adams,[2] Andrew R. Barron,[3] Mashitah M. Yusoff,[1] and Rajan Jose[1]

[1]Nanostructured Renewable Energy Materials Laboratory, Faculty of Industrial Science &Technology, Universiti Malaysia Pahang, Kuantan, 26300 Pahang, Malaysia.
[2] Department of Materials Science and Engineering, National University of Singapore, Singapore 117575, Singapore
[3] Energy Safety Research Institute, Swansea University, Bay Campus, Swansea, SA1 8QQ Wales, UK
*Corresponding author: rjose@ump.edu.my (R. Jose)

Abstract

This paper reports the synthesis of continuous nanobelts, whose thickness is less than half of its pore diameter, of a material hybrid composing of nanograins of nickel oxide and cobalt oxide by electrospinning technique and their capacitive charge storage properties. While the constituent binary metal oxides (NiO and Co_3O_4) formed solid cylindrical nanofibers the hybrid and a stoichiometric compound in the Ni-Co-O system, i.e., spinel-type $NiCo_2O_4$, formed as thin nanobelts due to the magnetic interaction between nickel and cobalt ions. The nanobelts showed six-fold larger surface area, wider pores, and impressive charge storage capabilities compared to the cylindrical fibres. The hybrid nanobelts showed high specific capacitance (C_S ~1250 F g^{-1} at 10 A g^{-1} in 6 M KOH) with high capacity retention, which is appreciably larger than found for the stoichiometric compound (~970 F g^{-1} at 10 A g^{-1}). It is shown that the hybrid nanobelts have lower internal resistance (1.3 Ω), higher diffusion coefficient (4.6×10^{-13} cm^2 s^{-1}) and smaller relaxation time (0.03 s) than the benchmark materials studied here.

Keywords: Nanocomposites; Hybrid metal oxides; Energy storage devices; Renewable energy; Electrochemical charge storage

Introduction

Hybrids of functional materials have long been synthesized for achieving enhanced physical and chemical properties. In this era of energy intensive electronics and electric vehicles, devices utilising hybrid materials are gaining increased importance as they could offer improved performance at a lower cost [1-4]. Furthermore, if the hybrid materials are synthesized in one-dimensional morphology at nanometer dimensions, electrical properties could be tailored [5, 6]. Hybrid properties are achieved through many methods such as physical mixing of its components, chemical methods such as core/shell, hierarchical structures, nanoparticle-decorated nanowires, and carbon-reinforced porous materials are few examples [7-13].

Considerable efforts have been made on fabricating electrochemical energy storage devices, such as batteries and electrochemical capacitors, utilising combined properties of hybrids [14-19]. Due to anisotropic electrical properties, nanowires (NWs) are a preferred choice as electrodes for energy storage; many nanowire systems are reported with excellent charge storage properties [20, 21]. A nanobelt morphology is preferred over nanowires of spherical cross-section because the former could offer higher surface-to-volume ratio and reduced diffusion path for ions in electrolyte creating better charge discharge rates [22]. Although there are few reports on the nanobelts of a single material system [23, 24], a nanobelt of a hybrid of two chemically distinct phases has not yet been reported.

Among the widely explored electrochemical materials as supercapacitor electrodes, NiO and Co_3O_4 received high attention owing to their high theoretical specific capacitance (C_S ~2570 and ~3560 F g^{-1}, respectively). Although Co_3O_4 based devices provide high C_S their inferior rate capability due to poor electrical conductivity (~10^{-3} S m^{-1}) poses an issue. On the other hand, NiO offers an order of magnitude higher conductivity (10^{-2} S m^{-1}) despite

its relatively lower C_S. There have been efforts to enhance electrochemical performance of Co_3O_4 by the addition of NiO [25-38]. Although improved C_S have been reported in many of these works, poor rate capability and device performance were still observed. As a solution to these shortcomings, in the present work, a hybrid of NiO–Co_3O_4 in the forms of continuous nanobelt (hybrid nanobelts, HNBs) has been synthesized by electrospinning technique [39]. Interestingly, the single component counterparts, i.e., NiO [40] and Co_3O_4 [41], formed as nanowires while the hybrid was nanobelts under similar electrospinning conditions. A stoichiometric compound ($NiCo_2O_4$) has also been synthesized as nanobelts; electrochemical characterization of the materials show that the HNBs show superior capacitive charge storage properties.

Experimental details

The NiO–Co_3O_4 hybrid was synthesized by electrospinning technique using a similar procedure adopted for their single component binary counterparts [40, 41] but with modifications. The main difference was in the amount of precursors: the metal precursors were used in 1:1 molar ratio for the synthesis of the NiO–Co_3O_4 hybrid (no other ratios led to a hybrid). Starting materials were cobalt acetate tetrahydrate, nickel acetate tetrahydrate and polyvinyl alcohol (PVA; Mw 145,000, Merck). For preparing HNBs, the precursors of cobalt and nickel taken in a 1:1 molar ratio were dissolved in 7wt.% of PVA solution. With slow and continuous stirring for 24 h, a clear solution was obtained. This clear solution was electrospun utilising a commercial electrospinning unit (Electroris, nanoLab, Malaysia). Electrospinning parameters were set as injection rate of 0.6 mL h^{-1}, voltage ~18 kV and aluminium foil collector at a distance 15 cm from the spinneret. The relative humidity around spinning unit was maintained at ~30%. The as-spun fibres were calcined at 450^oC for 1 h in air for removing the polymer and complete nucleation of nanohybrid. The single component binary metal oxide analogues (i.e., NiO and Co_3O_4) were synthesized as reported before [42].

In addition, a ternary stoichiometric compound, $NiCo_2O_4$, was also synthesized by electrospinning using a similar procedure except that stoichiometric amounts of Ni and Co precursors were dispersed in the PVA solution.

The viscosity of the polymeric solution used for electrospinning was measured using a rheometer (LVDV III Ultra, Brookfield Co.,USA). The crystal structures of the material were studied by X-ray diffraction (XRD) using a Rigaku Miniflex II X-ray diffractometer employing CuKα radiation (λ = 0.15406 nm). XRD analysis was carried out by putting the powder sample into the holder followed by pressing it lightly using a glass slide to obtain smooth flat surface and was scanned in the range 2θ = 20 to 70° with step size 0.02° and scan speed 1°/min. The morphology and microstructure of the materials were studied by scanning electron microscopy (7800F, FESEM, JEOL, USA). For this analysis the metal oxide samples were coated with gold (Au) using BIO-RAD Polaron Division SEM Coating System machine. This coating process was conducted under 0.1 mbar pressure and 30 mA for 75 seconds. The samples were then placed in the FESEM holder and were evacuated at a pressure of 5 bar. Measurements of Energy Dispersive X-ray Spectrometer (EDX) (using 7800F, FESEM, JEOL, USA) were carried out to determine the atomic and weight percentage of Ni and Co in HNBs and $NiCo_2O_4$ samples. Samples for transmission electron microscopy (TEM) analysis were prepared by ultrasonically dispersing the metal oxides in ethanol for 3 h. A drop of this solution was then allowed to dry on a carbon coated copper grid. Morphology of the materials and high resolution lattice images of the samples were obtained using TEM operating at 300 kV (FEI, Titan 80–300 kV). X-ray photoelectron spectroscopy (XPS) was performed using a PHI Quantera II (Physical Electronics) operating with an X-ray source of Al-Kα radiation at 100 W for the chemical analysis of the hybrid material. The survey spectra were recorded in the range 0 – 1327 eV at pass energy 120 eV with a resolution of 0.5 eV maintaining a low pressure of 10^{-10} Torr; high resolution spectra

were recorded with smaller constant pass energy of 20 eV with a resolution of 0.1 eV. Charge referencing was carried out against adventitious carbon, assuming its binding energy at 284.8 eV. The spectra were analysed using Origin 9.0 by fitting the high resolution spectra into multiple Gaussian curves; the baseline was modelled by adjacent averaging. Gas adsorption behaviour and BET surface area of the materials was determined using Micrometrics (Tristar, 3000) instrument in nitrogen atmosphere.

The electrodes for electrochemical studies were fabricated by coating slurry of the active material on pre-cleaned nickel foam substrates using acetone, HCl, water and ethanol. The slurry, in a typical experiment, was prepared by mixing the NiO–Co_3O_4 hybrid with polyvinylidenefluoride (PVDF) (Sigma Aldrich, USA) and carbon black (Super P conductive, Alfa Aesar, UK) in the ratio 75:10:15. N-methyl-2-pyrrolidinone (NMP), which works as a homogeniser, was added to the above mixture and stirred well for 24 h. The slurry thus obtained was pasted on the pre–cleaned nickel substrate (area ~1 cm^2) and dried at 60^oC. The dried electrode was subsequently pressed at a pressure of 5 ton using a hydraulic press. The active material loading on the electrodes was ~2.5 mg cm^{-2}. Electrodes of the binary metal oxide (NiO and Co_3O_4) analogues were also prepared in a similar way.

The cyclic voltammetry (CV), charge-discharge cycles (CDC), electrochemical impedance spectroscopy (EIS) measurements of the electrodes were studied using potentiostat-galvanostat (PGSTAT M101, Metrohm Autolab B.V., Netherlands) employing NOVA 1.9 software. The EIS measurements were carried out in the frequency range 100 kHz–0.01 Hz at respective open circuit potential. A platinum rod and a saturated Ag/AgCl electrode were used as the counter and the reference electrodes, respectively. Electrolyte used was 6M KOH because of its high ionic conductivity (~627 mS cm^{-1}).

Results and discussion

The FESEM images of the as-spun fibers of the polymeric solutions containing precursors in the 1:1 molar ratio (which developed the NiO–Co_3O_4 hybrid upon heating, hereafter termed as hybrid nanobelts, HNBs) and the one intended to prepare the stoichiometric compound, $NiCo_2O_4$, are shown in figure 1. The images show a bimodal distribution of fibre sizes and morphologies; small cylindrical fibers and large belt-like fibers. The belt-like fibers had a thickness up to ~900 nm, whereas the cylindrical ones had much smaller diameter (~200 – 300 nm). However, upon annealing they formed into nanobelts of thickness ~9 nm and average width of ~250 nm (figure 1 c-f). Interestingly, while the HNB and $NiCo_2O_4$ were nanobelts, their binary components, i.e., NiO [40] and Co_3O_4 [41], formed as nanowires with an average diameter of ~55 nm (*See supplementary information, figure S1*), under similar electrospinning conditions.

There are conflicting ideas regarding nanobelt formation during electrospinning [24, 43-45]. One of the ideas suggests that the thickness of as-prepared fibres could be tailored by changing the metal ion concentration of the initial polymeric solution, which upon annealing results in different morphologies such as fibres, belts or tubes [24]. Cheng et al. suggest that water evaporation rate and PVP burning rate during annealing of the polymeric fiber considerably influence the formation of different morphologies including nanobelts [46]. Another more general concept suggests tailoring of electrospinning parameters (such as viscosity, humidity, flow rate, applied voltage etc.) for obtaining different morphologies [44]. Formation of belt morphology has been explained as arising from a mechanical impact when thicker partly solidified gel-like fibres fall on the collector surface [44]. While few thicker as-spun fibers in figure 1 support this idea, a large fraction of as-spun fibers are cylindrical and the origin of belt-formation may be different.

For understanding the reason behind the belt formation in the present study, the viscosities of the spinning polymeric solutions were measured (Table 1). The viscosities of the nickel and cobalt precursor solutions were similar (~78 cP); surprisingly, the viscosity of their mixture is nearly doubled (147 cP). For further confirmation, the viscosity values of similar hybrid materials such as CuO–Co_3O_4 and CuO–NiO were measured; they neither showed such a considerable change in viscosity on mixing (Table 1) nor give a belt morphology (data not shown). However, increased viscosity alone could not trigger the transition into a belt-like morphology, because materials like SnO_2 shows wire morphology even when the precursor solution has much higher viscosities than the NiO–Co_3O_4 solution (250–350 cP) [47]. We could identify only one possible reason for this result, which is due to the magnetic interaction between the solvated Ni^{2+} and Co^{3+} ions [48]. Therefore, the magnetic interaction could be responsible for the belt morphology of the NiO–Co_3O_4 hybrid and $NiCo_2O_4$. The belt morphology would offer superior surface area than wire morphology. For example, assuming a dimension of ~1 μm length, the belts of the HNBs have ~6–fold larger surface area than wires, which has been confirmed using BET surface area measurements to be discussed later.

The morphology, surface, and lattice structure of the HNBs were further examined by TEM. Figure 2 (a&b) show the bright field TEM images of HNBs of different magnifications; the TEM images of the binary NWs can be found in figure S2 (*See supplementary information, figure S2)*. The belts are made up of small particles, whose size determined using the Image J software is ~10–15 nm. Particle packing appears to be tight, however, many bright regions composing pores of size <10 nm was observed. The partial transparency of the belts also indicates their nanometer sized thickness, which is not normally observed in nanowires (figure S2). The particle packing and their morphology is more obvious in a high resolution bright field image presented in figure 2b. The high resolution

TEM (HRTEM) images in figure 2c&d shows the lattice structure of the HNBs. Well crystallized as well as semi-amorphous regions were observed in HRTEM; the crystalline regions could be indexed to NiO and Co_3O_4 nanoparticles. In figure 2c, the lattice planes with 0.210 and 0.246 nm spacing were observed, which correspond to (200) plane of NiO and (311) plane of Co_3O_4, and in figure 2d, spacing of 0.146 and 0.445 corresponding to (220) plane of NiO and (111) plane of Co_3O_4, respectively. The lattice spacing was determined using the Image J software by considering at least 6 parallel planes composing a particle.

To characterise the crystal and chemical structures of the HNBs, XRD and XPS techniques were employed. Figure 3a shows the XRD patterns of HNBs compared with those of its individual components. It can be clearly seen that the peak positions of NiO and Co_3O_4 exactly match with those of HNBs without any shift, indicating the hybrid formation. All the XRD peaks corresponding to Co_3O_4 in the HNBs are sharper than they are in the single phase indicating a highly ordered phase. The XRD peaks of NiO correspond to a face centred cubic unit cell (Space group $Fm\bar{3}m$) with lattice parameters a = 0.418 nm which is in agreement with reported values (ICDD card No: 4-0835) and the Co_3O_4 peaks corresponds to the space group $Fd\bar{3}m$ with lattice parameter a = 0.805 nm (ICDD card No. 65-3103). It can be argued that a mixture of NiO and Co_3O_4 would favour the formation of the spinel-type stoichiometric compound, $NiCo_2O_4$. To examine this possibility, we have synthesized $NiCo_2O_4$ by electrospinning and compared their XRD patterns (figure 3b). Clearly a shift in peak position (up to ~1^o) can be observed between $NiCo_2O_4$ and HNBs, which rule out the above possibility. Besides, a compound formation in the composition meant for HNBs would show presence of unreacted NiO or Co_3O_4 in the XRD pattern. The graphs in figure S3 (a-d) compare the XRD patterns of HNBs with some of the reported compounds in the NiO–Co_3O_4 system reported literature such as $NiCoO_2$, CoO, CoO_2 and CoO_3 (*See supplementary*

information, figure S3), these materials could not be detected in the XRD pattern eliminating such possibilities.

To examine the chemical composition, the HNBs were further characterized by XPS. The survey spectrum in figure 4a shows that the primary constituents of HNBs are cobalt, nickel and oxygen. In figure 4b two peaks corresponding to Co $2p_{3/2}$ and Co $2p_{1/2}$ can be seen at 780.7 eV and 796.3 eV, respectively (full width half maximum (FWHM) values of fitted peaks), with a spin-energy separation of 15.6 eV, which corresponds to the earlier reported values [49]. The Co $2p_{3/2}$ and Co $2p_{1/2}$ were each fitted into two peaks as shown in figure 4b, which corresponds to Co^{3+} and Co^{2+} oxidation states. Similarly, while observing the peaks of Ni 2p XPS spectra as shown in figure 4c, there are two peaks corresponding to Ni $2p_{3/2}$ and Ni $2p_{1/2}$ at 855.3 eV and 872.8 eV, respectively (FWHM values of fitted peaks), with a spin-energy separation of 17.5 eV also in line with the reported literature [50]. One satellite peak each was observed near Ni $2p_{3/2}$ and Ni $2p_{1/2}$ peaks indicated presence of Ni^{2+} in pure NiO phase. The XPS spectrum of oxygen (O 1s) in figure 4d suggests that generally 2^- charge is associated with the oxygen present in the range of 530.2–532.3 eV, which corresponds to Co_3O_4 and NiO; presence of $NiCo_2O_4$ would have resulted in additional satellite peaks in the O 1s spectra [51, 52]. EDX analysis was also conducted to confirm the difference in percentage of composition of elements in HNBs and $NiCo_2O_4$ materials. The results (shown in Table 2 and figure S4) verify the findings from XRD and XPS analysis that the atomic ratio of HNBs is ~1:1 and that of $NiCo_2O_4$ is 2:1.

Surface properties of the materials were studied by nitrogen adsorption-desorption measurement. The nitrogen adsorption isotherms of all the samples are shown in figure S5 (a-d). BET surface area, total pore volume, and average pore diameter of the materials determined from the adsorption measurements are listed in Table 3. It can be seen that the surface area of the HNBs (~79 m^2g^{-1}) are similar to the $NiCo_2O_4$ samples (~70 m^2g^{-1}) and

much higher than their binary analogues (~14 m^2g^{-1}). i.e., measured surface are of the nanobelts were over 5-fold larger than their binary analogues as predicted from the SEM images. This higher surface area of the samples is reflected in the superior electrochemical properties, such as capacitive rate capability, which is to be discussed later. The inset of the BET curves shows the presence of micro, meso and macropores, suggesting improved solvated ion intercalation and larger accessible surface area which results in improved electrochemical properties [53]. Comparatively, pore diameter (~21 nm) and specific pore volume (0.5 cm^3g^{-1}) were higher in the case of HNBs than the $NiCo_2O_4$ nanobelts (pore diameter ~17 nm and pore volume ~0.3 cm^3g^{-1}) and binary analogues (pore diameter ~11 nm and pore volume ~0.5 cm^3g^{-1}), which is possibly a source of its larger surface area. Interestingly, the pore diameter of the HNBs (~ 21 nm) is more than double the thickness of the belts (~10 nm), consistent with the observations from TEM studies. The pore size of HNBs is larger than the solvated ion size of many electrolytes [43]; and therefore, HNBs would offer unique advantages when they are used for electrochemical applications.

Galvanostatic charge-discharge cycling (CDC) studies were employed to analyze the practically achievable C_S, internal resistance, and long term cyclability of the electrodes. The discharge curves at 10 A g^{-1} of HNBs, $NiCo_2O_4$ and component metal oxides can be seen in figure 5a. The discharge curves of battery-type electrodes are usually as a result of three processes (figure 5b, discharge curves of HNBs at different current densities): (i) an abrupt initial potential drop due to the surface contribution of the PC (ii) a slow potential decay through deep intercalation, and (iii) relatively faster voltage drop indicating EDLC mechanism. It was observed that all the electrodes were showing a maximum potential of 0.4 V in 6 M KOH electrolyte. The nonlinear shape of discharge curve suggests that faradaic reactions are predominant in the electrodes. Evidently, the discharge time increased considerably for HNBs when compared to $NiCo_2O_4$, Co_3O_4 and NiO. The variation of

specific capacitance with current density of all materials studied can be observed in figure 5c. The C_S of the electrodes at ~10 A g^{-1} are 416, 611, 1251 and 970 Fg^{-1} for NiO, Co_3O_4, HNBs and $NiCo_2O_4$ respectively. Similar C_S has been reported for electrospun $NiCo_2O_4$ nanobelts (~800 F g^{-1}) in a previous publication [24]. The HNBs showed the highest C_S with fairly high rate capability, which could be ascribed to their lower thickness than their pore size. On the other hand, the C_S of cylindrical fibres of NiO and Co_3O_4, whose diameters are much higher than their pore size, decreased substantially at higher current densities. Evidently, the C_S decreased only 11% with current density increasing from 1 A g^{-1} to 10 A g^{-1} in the case of HNBs, in comparison to 15%, 40% and 36% decrease for $NiCo_2O_4$, Co_3O_4 and NiO respectively. The ultra-thin belt morphology with larger pores is expected to facilitate the diffusion of OH^- ions thereby accessing more active sites which in turn enhance the capacitance. Figure 5d shows the charge–discharge cycle of HNBs from which equivalent series resistance (ESR) could be reliably calculated [9]. The potential drop (V_{IR}) between the charge and discharge curves is a measure of the ESR of the electrodes. The factors contributing the ESR are (i) intrinsic resistance of the electro-active material, (ii) electrolyte resistance, and (iii) the contact resistance at the active material–current collector interface. The ratio of potential drop (V_{IR}) to the discharge current (I_D) of the electrode gave ESR values as: NiO – 1.4 Ω, Co_3O_4 – 1.7 Ω, HNBs – 1.2 Ω and $NiCo_2O_4$ – 1.3 Ω. Thus, the ESR of the HNBs is lower than that of its constituents and compound thereby offering improved capacitive performance. The reversibility and extended cyclability of the electrode can be determined from the CD curves by calculating the coulombic efficiency (η), which is defined as the ratio of discharging to the charging time. The η of HNBs was 95% which is superior to that observed for single components (92%). The operational stability of the HNBs was evaluated by galvanostatic charge-discharge testing at a current rating of ~10 A g^{-1}. Retention

in capacitance and η of ~99 % was shown by HNBs at the end of the 5000 cycle test program (figure 6).

Cyclic voltammetry (CV) was employed to determine the nature of the oxidation reduction reactions occurs in the electrodes giving rise to the above discharge capacitance. Figure 7a displays the CV curves of HNBs, $NiCo_2O_4$, and their constituent binaries, respectively, at a scan rate of 5 mVs^{-1}. The cathodic and anodic peaks, arising due to oxidation and reduction reactions, illustrate the battery-type behaviour of materials which is also supported by the non-linear variation of current with scan rate in the charge – discharge cycling. The voltammetric current of HNBs is much higher than the benchmark materials indicating its superior electrochemical performance. The electrochemical reactions (1 to 3) of the electrodes containing NiO and Co_3O_4 are routinely expressed as [41, 54]:

$$NiO + OH^- \leftrightarrow NiOOH + e^- \quad (1)$$

$$Co_3O_4 + 4H_2O + 2e^- \leftrightarrow 3Co(OH)_2 + 2\,OH^- \quad (2)$$

$$3CoOOH + e^- \leftrightarrow Co_3O_4 + OH^- + H_2O \quad (3)$$

However, these relations alone cannot explain the observed C_S because the HNBs and $NiCo_2O_4$ showed significantly different discharge capacitances. While comparing the oxidation peaks of HNBs and $NiCo_2O_4$, one would observe that the peak in HNB is shifted to more negative potential than $NiCo_2O_4$ which in turn lower than their constituents. Usually oxidation at lower potential occurs for materials of higher electrical conductivity [40, 41]; a lowered internal resistance of HNBs was also observed from the charge – discharge cycling curves. However, a scan rate dependent CV analysis shows (*See supplementary information, figure S6 a*) a shift in peak position towards the higher potentials indicating the charge polarization at the electrode – electrolyte surface. The variation of C_S with scan rate is

analysed (*See supplementary information, figure S6 b*) and HNBs showed highest capacitance value, similar to that as observed from CDC. To compare the relative advantage of the HNBs on the charge diffusion to the electrode, we compared the extent of faradaic reaction from the variation of scan rate (v) with voltammetric current (i). If the current arises from bulk intercalation process, it follows diffusion kinetics and the current i varies as $v^{1/2}$ (battery-type). On the contrary, if the current arises from surface charge storage processes (pseudocapacitance), a linear relation with v can be observed. As can be observed from figure 7b, all the materials show $i \propto v^{1/2}$ relationship, suggesting dominance of bulk intercalation charge storage processes. Further, the slope of such a line is proportional to the charge diffusion according to the Randles-Sevcik equation (5) ,

$$i = 2.69 \times 10^5 \times n^{3/2} \times D^{1/2} \times A \times C_0 \times \sqrt{v} \qquad (4)$$

where n is the number of electron transferred to the electrode surface, A is the surface area of the electrode, D is the ion diffusion coefficient, v is the scan rate, and C_0 is the initial ion concentration. One would observe that the HNBs show the largest slope thereby offering superior charge diffusion process through the electrode. The Ds calculated using the slope of i vs $v^{1/2}$ graph is in Table 4. Highest value of D (4.6×10^{-13} cm^2s^{-1}) is observed for HNBs which suggests an improved rate of ion transport and, consequently, relatively lower electrode polarization during charge–discharge process [55, 56]. On the other hand, the Ds of NiO, Co_3O_4 and $NiCo_2O_4$ are 1.9×10^{-13}, 5.3×10^{-14} and 3.4×10^{-13} cm^2s^{-1}, respectively. These Ds could be directly correlated to their pore sizes – the larger is the pore size the larger is the D. Besides pore size, electrical conductivity of the electrodes also influence the D [43]. For example, Co_3O_4 has the lowest D and electrical conductivity (Table 4) but NiO with similar pore size has an order of magnitude higher D due to its higher electrical conductivity.

Therefore, one could argue from the improved D and C_S of the HNBs that a synergistic combination has been achieved.

To further correlate surface properties and C_S, the quantity of electrochemically active sites in the electrodes accessed by the solvated ions (n) in the electrolyte, which varies with scan rates, was calculated following the equation (6),

$$n = \frac{C_S \times m \times \Delta V}{F \times Z} \quad (5)$$

where 'm' is the molecular weight, ΔV is the redox potential, F is the Faraday's constant and Z is the oxidation state of the electrode material. The n for $NiCo_2O_4$ and HNBs at 2 mV s^{-1} were ~29 and ~34%, respectively. i.e., the hybrid contributed more electrochemically active surface. This explains the higher C_S values attained by HNBs. Electrochemical reversibility of the material, i.e., the coulombic efficiency (η), was calculated from the ratio of the area of the anodic to the cathodic peaks of CV curves. The η measured from scan rate (2 mV s^{-1}) of HNB electrodes show the highest value (97%) compared to the other electrodes indicating improved electrochemical reversibility and better capacity retention for long cycle of operation. The CV measurements, thereby, show that the HNBs could offer improved capacitance, electrochemical active sites and coulombic efficiency than the benchmark materials studied here.

Electrochemical impedance spectroscopy (EIS) provides a powerful technique to study the charge kinetics at an electrode – electrolyte interface. Figure 8a compares the Nyquist plots of the electrodes fitted using a standard Randles circuit routinely used for evaluation of the supercapacitor electrodes. The equivalent circuit (inset figure 8a) is a series and parallel combination of device bulk resistance (R_S), charge transfer resistance (R_{CT}), electric double layer capacitance (C_d), Warburg impedance (Z_W), and a constant phase

element (CPE_{PC}) representing the supercapacitance dispersion on the nickel foam owing to the surface irregularities [57, 58]. The charge kinetic parameters thus determined for HNBs are R_S = 1.2 Ω, R_{CT} = 1.1 Ω, C_d = 1.5 mF, Z_W = 220 mMho and Z_{CPE} = 39.5 $(mFs)^{1/n}$ (n = 0.92). The HNBs showed lowest R_{CT} value (1.1 Ω) followed by $NiCo_2O_4$ (1.2 Ω), NiO (1.3 Ω) and Co_3O_4 (1.5 Ω) respectively. A low R_{CT} of HNBs sample indicates enhanced ionic conductivity and electrolyte diffusion through the pores of the electrode and would lead to improved rate capability [59]. The measured kinetic parameters corroborate the results obtained from CV and CDC analysis that HNBs have superior electrochemical properties than the other materials under study (Table 4). The responsiveness of the supercapacitors are measured in terms of the charge relaxation time (τ) or RC time constant, which is defined as the time required dissipating half of the energy stored. To determine value of τ, plot of frequency vs phase difference was drawn (figure 8b) from which the characteristic frequency ($f_0 = \frac{1}{\tau}$) (the point at which the circuit is equally capacitive and resistive) is calculated [60]. The phase angle is 90^o for an ideal capacitor and 45^o when the capacitive and resistive impedances are equal. A phase angle of 90^o is typically observed only in EDLCs using carbon materials whereas deviations from 90^o are commonly observed in pseudocapacitors. The phase angles of all the four materials are compared in figure 8b. The f_o is 25.86 Hz in HNBs, which is much higher than the conventional activated carbon (~0.05 Hz) [61], whereas that of $NiCo_2O_4$, NiO and Co_3O_4 is 10.29, 2.09 and 0.22 Hz, respectively. As observed from figure 8b HNBs show highest f_o, which means that the HNB electrode remains capacitive for a wider frequency range. The τ value, which measures how fast a supercapacitor is discharged and is related to power density of supercapacitors, are much lower for HNBs (0.03 s) when compared to the other three electrodes. This rapid frequency response of the HNBs electrode would provide superior rate capability and cycling stability

in practical devices. Comparison of these charge kinetic parameters of component and hybrid electrodes indicates the superiority of HNBs electrodes.

Conclusions

In conclusion, we have electrospun continuous nanobelts of a hybrid material, in which NiO and Co_3O_4 remain chemically intact. Thickness of the NiO–Co_3O_4 hybrid is less than half of its porosity. The hybrid and a stoichiometric compound in the Ni-Co-O system, i.e., spinal-type $NiCo_2O_4$ crystallized as belts whereas their constituent binary metal oxides (NiO and Co_3O_4) formed as solid cylindrical nanofibers. Formation of belts is thought to originate from the magnetic interaction between nickel and cobalt ions. Then hybrid nanobelts show superior charge storage properties primarily owing to its superior surface area and porosity as well as improved electrical conductivity. Besides, the porosity of the hybrid nanofibers, which is two times higher than the thickness of the belt, was helpful in achieving large ion diffusion coefficient and consequently large fraction of its electrochemically active surface. The hybrid nanofibers have a specific capacitance much higher than that of the stoichiometric $NiCo_2O_4$ and constituent binary metal oxides.

Acknowledgements: This project was funded by the Research & Innovation Department of Universiti Malaysia Pahang (RDU1503100 and GRS 150328).

References

[1] E. Baek, S. Pregl, M. Shaygan, L. Römhildt, W.M. Weber, T. Mikolajick, D.A. Ryndyk, L. Baraban, G. Cuniberti, Optoelectronic switching of nanowire-based hybrid organic/oxide/semiconductor field-effect transistors, Nano Research, 8 (2015) 1229-1240.
[2] M.M. Mohamed, S.A. Ahmed, Pd-doped β-Bi2O3/Bi2Sn2O7 hybrid nanocomposites for photocatalytic fluorene oxidation: A green approach for the synthesis of fluorenone/fluorenol mixture, Microporous Mesoporous Mater., 204 (2015) 62-72.
[3] S. Gupta Chatterjee, S. Chatterjee, A.K. Ray, A.K. Chakraborty, Graphene–metal oxide nanohybrids for toxic gas sensor: A review, Sensors and Actuators B: Chemical, 221 (2015) 1170-1181.

[4] N. Mhlanga, S.S. Ray, Kinetic models for the release of the anticancer drug doxorubicin from biodegradable polylactide/metal oxide-based hybrids, Int. J. Biol. Macromol., 72 (2015) 1301-1307.
[5] Z. Gui, E. Gillette, J. Duay, J. Hu, N. Kim, S.B. Lee, Co-electrodeposition of RuO2-MnO2 nanowires and the contribution of RuO2 to the capacitance increase, Phys. Chem. Chem. Phys., 17 (2015) 15173-15180.
[6] G.H. Jeong, S. Baek, S. Lee, S.-W. Kim, Metal Oxide/Graphene Composites for Supercapacitive Electrode Materials, Chemistry – An Asian Journal, 11 (2016) 949-964.
[7] D.P. Dubal, O. Ayyad, V. Ruiz, P. Gomez-Romero, Hybrid energy storage: the merging of battery and supercapacitor chemistries, Chem. Soc. Rev., 44 (2015) 1777-1790.
[8] H. Wang, J. Guo, C. Qing, D. Sun, B. Wang, Y. Tang, Novel topotactically transformed carbon-CoO-NiO-NiCo(2)O(4) nanosheet hybrid hetero-structured arrays as ultrahigh performance supercapacitors, Chem. Commun., 50 (2014) 8697-8700.
[9] D.E. Lobo, P.C. Banerjee, C.D. Easton, M. Majumder, Miniaturized Supercapacitors: Focused Ion Beam Reduced Graphene Oxide Supercapacitors with Enhanced Performance Metrics, Adv. Energy Mater., 5 (2015) 1500665-n/a.
[10] Z.-D. Huang, K. Zhang, T.-T. Zhang, X. Li, R.-Q. Liu, X.-M. Feng, Y. Li, X.-J. Lin, Y.-B. He, X.-S. Yang, Y.-W. Ma, Hierarchical dispersed multi-phase nickel cobalt oxide mesoporous thorn microspheres as superior rate anode materials for lithium ion batteries, J. Mater. Chem. A, 3 (2015) 20886-20891.
[11] X. Hui, L. Qian, G. Harris, T. Wang, J. Che, Fast fabrication of NiO@graphene composites for supercapacitor electrodes: Combination of reduction and deposition, Mater. Des., 109 (2016) 242-250.
[12] J. Yang, C. Zeng, F. Wei, J. Jiang, K. Chen, S. Lu, Cobalt–carbon derived from zeolitic imidazolate framework on Ni foam as high-performance supercapacitor electrode material, Mater. Des., 83 (2015) 552-556.
[13] P. Jiang, Q. Wang, J. Dai, W. Li, Z. Wei, Fabrication of NiO@Co3O4 core/shell nanofibres for high-performance supercapacitors, Mater. Lett., 188 (2017) 69-72.
[14] A.K. Singh, D. Sarkar, G. Gopal Khan, K. Mandal, Designing one dimensional Co-Ni/Co3O4-NiO core/shell nano-heterostructure electrodes for high-performance pseudocapacitor, Appl. Phys. Lett., 104 (2014) 133904.
[15] S.E. Chun, B. Evanko, X. Wang, D. Vonlanthen, X. Ji, G.D. Stucky, S.W. Boettcher, Design of aqueous redox-enhanced electrochemical capacitors with high specific energies and slow self-discharge, Nat. Commun., 6 (2015) 7818.
[16] S.G. Krishnan, M.V. Reddy, M. Harilal, B. Vidyadharan, I.I. Misnon, M.H.A. Rahim, J. Ismail, R. Jose, Characterization of MgCo2O4 as an electrode for high performance supercapacitors, Electrochim. Acta, 161 (2015) 312-321.
[17] H. Xu, J. Zhuang, Y. Chen, J. Wu, J. Zhang, Preparation and performance of Co3O4–NiO composite electrode material for supercapacitors, RSC Adv., 4 (2014) 15511.
[18] C. Long, M. Zheng, Y. Xiao, B. Lei, H. Dong, H. Zhang, H. Hu, Y. Liu, Amorphous Ni-Co Binary Oxide with Hierarchical Porous Structure for Electrochemical Capacitors, ACS Appl. Mater. Interfaces, 7 (2015) 24419-24429.
[19] R. Jose, S.G. Krishnan, B. Vidyadharan, I.I. Misnon, M. Harilal, R.A. Aziz, J. Ismail, M.M. Yusoff, Supercapacitor Electrodes Delivering High Energy and Power Densities, Materials Today: Proceedings, 3 (2016) S48-S56.
[20] L. Mai, X. Tian, X. Xu, L. Chang, L. Xu, Nanowire electrodes for electrochemical energy storage devices, Chem. Rev., 114 (2014) 11828-11862.
[21] R.B. Pujari, A.C. Lokhande, A.A. Yadav, J.H. Kim, C.D. Lokhande, Synthesis of MnS microfibers for high performance flexible supercapacitors, Materials & Design, 108 (2016) 510-517.

[22] F.L. Zheng, G.R. Li, Y.N. Ou, Z.L. Wang, C.Y. Su, Y.X. Tong, Synthesis of hierarchical rippled Bi(2)O(3) nanobelts for supercapacitor applications, Chem. Commun., 46 (2010) 5021-5023.
[23] A.K. Mondal, D. Su, S. Chen, X. Xie, G. Wang, Highly porous NiCo2O4 Nanoflakes and nanobelts as anode materials for lithium-ion batteries with excellent rate capability, ACS Appl. Mater. Interfaces, 6 (2014) 14827-14835.
[24] L. Li, S. Peng, Y. Cheah, P. Teh, J. Wang, G. Wee, Y. Ko, C. Wong, M. Srinivasan, Electrospun porous NiCo2O4 nanotubes as advanced electrodes for electrochemical capacitors, Chemistry, 19 (2013) 5892-5898.
[25] K. Jang, S. Yu, S.-H. Park, H.-S. Kim, H. Ahn, Intense pulsed light-assisted facile and agile fabrication of cobalt oxide/nickel cobaltite nanoflakes on nickel-foam for high performance supercapacitor applications, J. Alloys Compd., 618 (2015) 227-232.
[26] G. Wang, L. Zhang, J. Kim, J. Zhang, Nickel and cobalt oxide composite as a possible electrode material for electrochemical supercapacitors, J. Power Sources, 217 (2012) 554-561.
[27] S.-K. Chang, Z. Zainal, K.-B. Tan, N.A. Yusof, W.M.D.W. Yusoff, S.R.S. Prabaharan, Nickel–cobalt oxide/activated carbon composite electrodes for electrochemical capacitors, Curr. Appl. Phys, 12 (2012) 1421-1428.
[28] M. Li, J.P. Cheng, F. Liu, X.B. Zhang, 3D-architectured nickel–cobalt–manganese layered double hydroxide/reduced graphene oxide composite for high-performance supercapacitor, Chem. Phys. Lett., 640 (2015) 5-10.
[29] X. Wang, X. Han, M. Lim, N. Singh, C.L. Gan, M. Jan, P.S. Lee, Nickel Cobalt Oxide-Single Wall Carbon Nanotube Composite Material for Superior Cycling Stability and High-Performance Supercapacitor Application, J. Phys. Chem. C, 116 (2012) 12448-12454.
[30] K. Wang, Z. Zhang, X. Shi, H. Wang, Y. Lu, X. Ma, Temperature-dependent self-assembly of NiO/Co3O4 composites for supercapacitor electrodes with good cycling performance: from nanoparticles to nanorod arrays, RSC Adv., 5 (2015) 1943-1948.
[31] L. Huang, D. Chen, Y. Ding, S. Feng, Z.L. Wang, M. Liu, Nickel-cobalt hydroxide nanosheets coated on NiCo2O4 nanowires grown on carbon fiber paper for high-performance pseudocapacitors, Nano letters, 13 (2013) 3135-3139.
[32] J. Cheng, Y. Lu, K. Qiu, H. Yan, J. Xu, L. Han, X. Liu, J. Luo, J.K. Kim, Y. Luo, Hierarchical Core/Shell NiCo2O4@NiCo2O4 Nanocactus Arrays with Dual-functionalities for High Performance Supercapacitors and Li-ion Batteries, Sci. Rep., 5 (2015) 12099.
[33] A. Sivanantham, P. Ganesan, S. Shanmugam, Hierarchical NiCo2S4 Nanowire Arrays Supported on Ni Foam: An Efficient and Durable Bifunctional Electrocatalyst for Oxygen and Hydrogen Evolution Reactions, Adv. Funct. Mater., 26 (2016) 4661-4672.
[34] A.S. Adekunle, K.I. Ozoemena, B.O. Agboola, MWCNTs/metal (Ni, Co, Fe) oxide nanocomposite as potential material for supercapacitors application in acidic and neutral media, J. Solid State Electrochem., 17 (2013) 1311-1320.
[35] T.M. Masikhwa, M.J. Madito, D. Momodu, A. Bello, J.K. Dangbegnon, N. Manyala, High electrochemical performance of hybrid cobalt oxyhydroxide/nickel foam graphene, J. Colloid Interface Sci., 484 (2016) 77-85.
[36] G.A.M. Ali, O.A. Fouad, S.A. Makhlouf, M.M. Yusoff, K.F. Chong, Co3O4/SiO2 nanocomposites for supercapacitor application, J. Solid State Electrochem., 18 (2014) 2505-2512.
[37] G. George, S. Anandhan, Synthesis and characterisation of nickel oxide nanofibre webs with alcohol sensing characteristics, RSC Adv., 4 (2014) 62009-62020.
[38] G. George, L. Elias, A.C. Hegde, S. Anandhan, Morphological and structural characterisation of sol–gel electrospun Co3O4nanofibres and their electro-catalytic behaviour, RSC Adv., 5 (2015) 40940-40949.

[39] S. Thenmozhi, N. Dharmaraj, K. Kadirvelu, H.Y. Kim, Electrospun nanofibers: New generation materials for advanced applications, Materials Science and Engineering: B, 217 (2017) 36-48.
[40] B. Vidhyadharan, N.K.M. Zain, I.I. Misnon, R.A. Aziz, J. Ismail, M.M. Yusoff, R. Jose, High performance supercapacitor electrodes from electrospun nickel oxide nanowires, J. Alloys Compd., 610 (2014) 143-150.
[41] B. Vidyadharan, R.A. Aziz, I.I. Misnon, G.M. Anil Kumar, J. Ismail, M.M. Yusoff, R. Jose, High energy and power density asymmetric supercapacitors using electrospun cobalt oxide nanowire anode, J. Power Sources, 270 (2014) 526-535.
[42] B. Vidhyadharan, I.I. Misnon, R.A. Aziz, K.P. Padmasree, M.M. Yusoff, R. Jose, Superior supercapacitive performance in electrospun copper oxide nanowire electrodes, J. Mater. Chem. A, 2 (2014) 6578.
[43] S. Yang, Y. Gong, Z. Liu, L. Zhan, D.P. Hashim, L. Ma, R. Vajtai, P.M. Ajayan, Bottom-up approach toward single-crystalline VO2-graphene ribbons as cathodes for ultrafast lithium storage, Nano letters, 13 (2013) 1596-1601.
[44] G. Li, Z. Hou, C. Peng, W. Wang, Z. Cheng, C. Li, H. Lian, J. Lin, Electrospinning Derived One-Dimensional LaOCl: Ln3+ (Ln = Eu/Sm, Tb, Tm) Nanofibers, Nanotubes and Microbelts with Multicolor-Tunable Emission Properties, Adv. Funct. Mater., 20 (2010) 3446-3456.
[45] L. Zhang, J. Hu, A.A. Voevodin, H. Fong, Synthesis of continuous TiC nanofibers and/or nanoribbons through electrospinning followed by carbothermal reduction, Nanoscale, 2 (2010) 1670-1673.
[46] Y. Cheng, B. Zou, C. Wang, Y. Liu, X. Fan, L. Zhu, Y. Wang, H. Ma, X. Cao, Formation mechanism of Fe2O3 hollow fibers by direct annealing of the electrospun composite fibers and their magnetic, electrochemical properties, CrystEngComm, 13 (2011) 2863.
[47] Q. Wali, A. Fakharuddin, I. Ahmed, M.H. Ab Rahim, J. Ismail, R. Jose, Multiporous nanofibers of SnO2 by electrospinning for high efficiency dye-sensitized solar cells, J. Mater. Chem. A, 2 (2014) 17427-17434.
[48] S. Kotler, N. Akerman, N. Navon, Y. Glickman, R. Ozeri, Measurement of the magnetic interaction between two bound electrons of two separate ions, Nature, 510 (2014) 376-380.
[49] L. Wang, B. Liu, S. Ran, H. Huang, X. Wang, B. Liang, D. Chen, G. Shen, Nanorod-assembled Co3O4 hexapods with enhanced electrochemical performance for lithium-ion batteries, Journal of Materials Chemistry, 22 (2012) 23541-23546.
[50] M.A. Peck, M.A. Langell, Comparison of Nanoscaled and Bulk NiO Structural and Environmental Characteristics by XRD, XAFS, and XPS, Chem. Mater., 24 (2012) 4483-4490.
[51] S. Jeong, S. Park, J. Cho, High-Performance, Layered, 3D-LiCoO2 Cathodes with a Nanoscale Co3O4 Coating via Chemical Etching, Adv. Energy Mater., 1 (2011) 368-372.
[52] J.G. Kim, D.L. Pugmire, D. Battaglia, M.A. Langell, Analysis of the NiCo2O4 spinel surface with Auger and X-ray photoelectron spectroscopy, Applied Surface Science, 165 (2000) 70-84.
[53] I.I. Misnon, R.A. Aziz, N.K.M. Zain, B. Vidhyadharan, S.G. Krishnan, R. Jose, High performance MnO2 nanoflower electrode and the relationship between solvated ion size and specific capacitance in highly conductive electrolytes, Mater. Res. Bull., 57 (2014) 221-230.
[54] M.-S. Wu, H.-H. Hsieh, Nickel oxide/hydroxide nanoplatelets synthesized by chemical precipitation for electrochemical capacitors, Electrochim. Acta, 53 (2008) 3427-3435.
[55] H. Liu, J. Wang, Hydrothermal Synthesis and Electrochemical Performance of MnCo2O4 Nanoparticles as Anode Material in Lithium-Ion Batteries, J. Electron. Mater., 41 (2012) 3107-3110.
[56] P. Simon, Y. Gogotsi, B. Dunn, Where Do Batteries End and Supercapacitors Begin?, Science, 343 (2014) 1210-1211.

[57] S.-B. Yoon, J.-P. Jegal, K.C. Roh, K.-B. Kim, Electrochemical impedance spectroscopic investigation of sodium ion diffusion in MnO2 using a constant phase element active in desired frequency ranges, J. Electrochem. Soc., 161 (2014) H207-H213.
[58] A.C. Nwanya, S.U. Offiah, I.C. Amaechi, S. Agbo, S.C. Ezugwu, B.T. Sone, R.U. Osuji, M. Maaza, F.I. Ezema, Electrochromic and electrochemical supercapacitive properties of Room Temperature PVP capped Ni(OH)2/NiO Thin Films, Electrochim. Acta, 171 (2015) 128-141.
[59] Q. Shao, J. Tang, Y. Lin, J. Li, F. Qin, K. Zhang, J. Yuan, L.-C. Qin, Ionic liquid modified graphene for supercapacitors with high rate capability, Electrochim. Acta, 176 (2015) 1441-1446.
[60] M.F. El-Kady, V. Strong, S. Dubin, R.B. Kaner, Laser scribing of high-performance and flexible graphene-based electrochemical capacitors, Science, 335 (2012) 1326-1330.
[61] K. Sheng, Y. Sun, C. Li, W. Yuan, G. Shi, Ultrahigh-rate supercapacitors based on eletrochemically reduced graphene oxide for ac line-filtering, Sci. Rep., 2 (2012) 247.

Table 1

Viscosities of the electrospinning polymeric solutions

Material	Morphology	Solution viscosity (cP)
Co_3O_4	nanowire	77.6
NiO	nanowire	77.8
NiO–Co_3O_4	nanobelts	146.5
NiO–CuO	nanowire	78.1
Co_3O_4–CuO	nanowire	78.4

Table 2
Atomic and weight percentage data from EDX analysis

NiO–Co_3O_4			$NiCo_2O_4$		
Element	Weight%	Atomic%	Element	Weight%	Atomic%
O K	23.9	53.6	O K	22.2	51.2
Co L	37.1	22.5	Co L	52.4	32.8
Ni L	38.9	23.8	Ni L	25.3	15.9
Total	100		Total	100	

Table 3
Surface properties of materials from BET analysis

Materials	Surface area (m^2g^{-1})	Pore volume (cm^3g^{-1})	Mean pore size (nm)
NiO	13.7	0.54	10.6
Co_3O_4	13.5	0.49	11.2
$NiCo_2O_4$	70.1	0.33	17.2
NiO–Co_3O_4	78.7	0.46	21.1

Table 4
Kinetic parameters of the electrodes obtained from CDC, CV and EIS analysis

	ESR (Ω)	D ($cm^2 s^{-1}$)	R_{CT} (Ω)	f_0 (Hz)	τ (s)
NiO	1.4	1.9×10^{-13}	1.3	2.1	0.48
Co_3O_4	1.7	5.3×10^{-14}	1.5	0.2	4.54
$NiCo_2O_4$	1.3	3.4×10^{-13}	1.2	10.3	0.09
NiO–Co_3O_4	1.2	4.6×10^{-13}	1.1	25.9	0.03

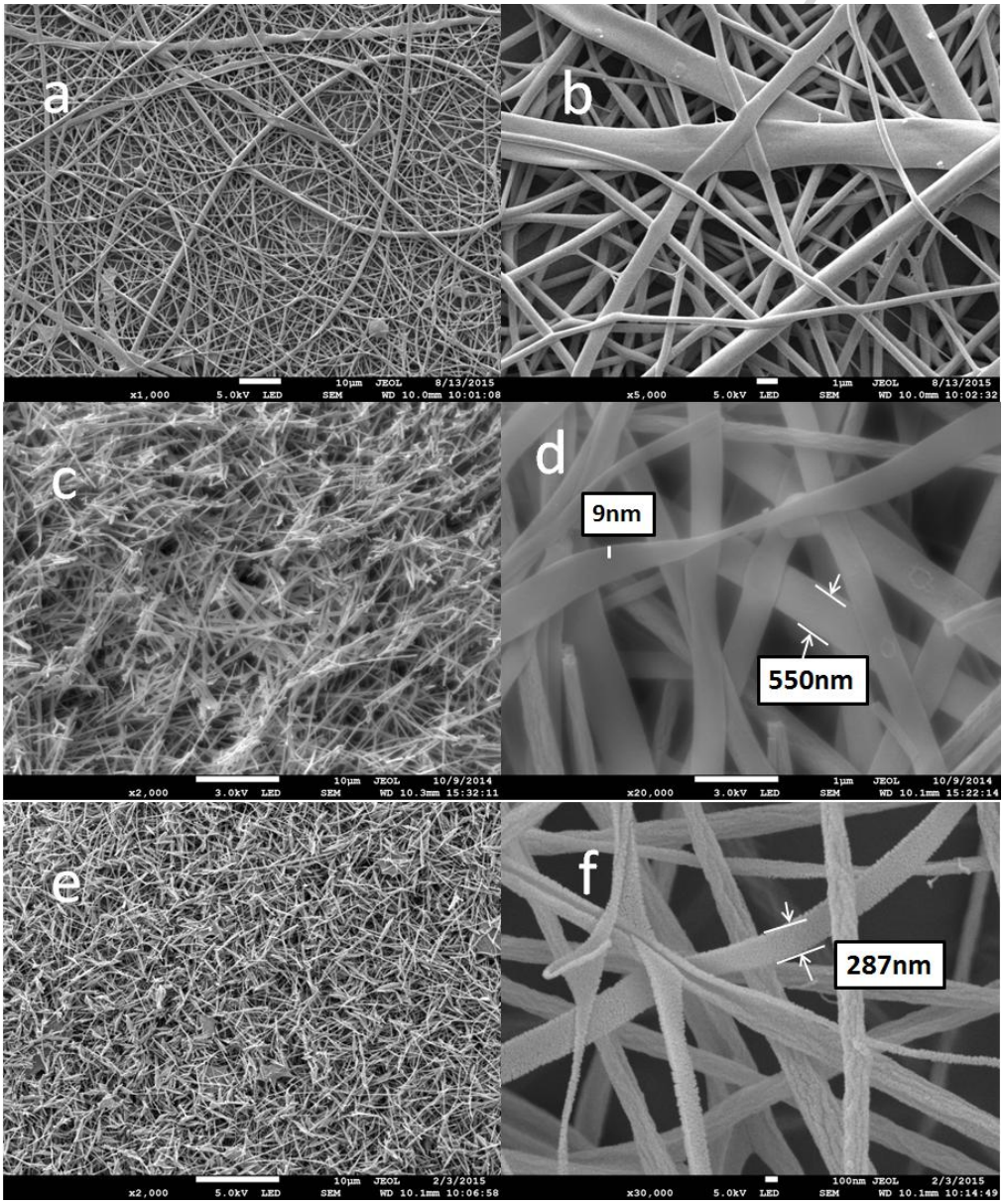

Figure 1. FESEM images of (a,b) as-spun fibers; (c,d) NiO–Co_3O_4 nanobelts; (e,f) $NiCo_2O_4$ nanobelts.

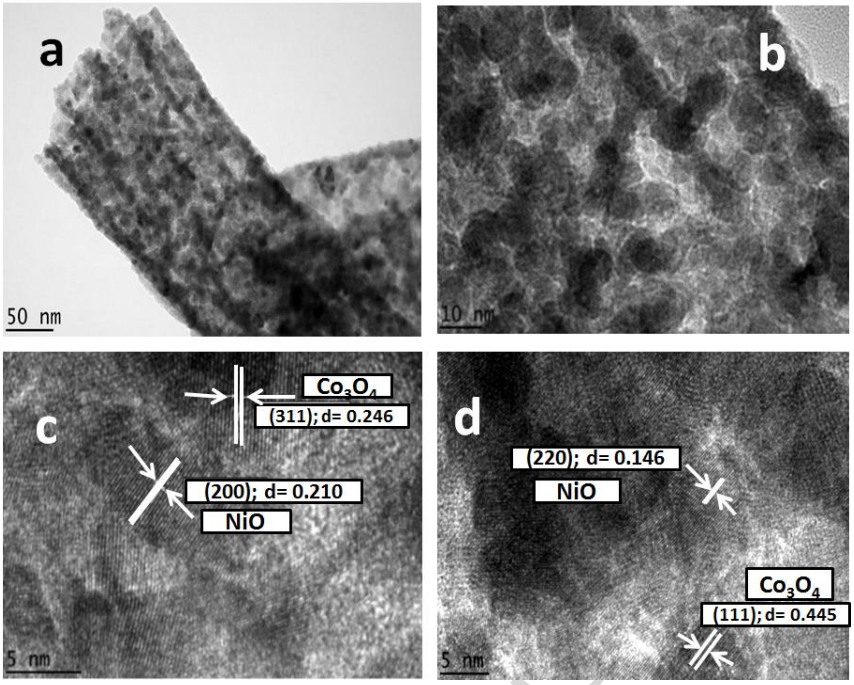

Figure 2. (a,b) TEM images of NiO–Co_3O_4 nanobelts; (c,d) HRTEM images of NiO–Co_3O_4 nanobelts with lattice planes indexed to their constituent metal oxides

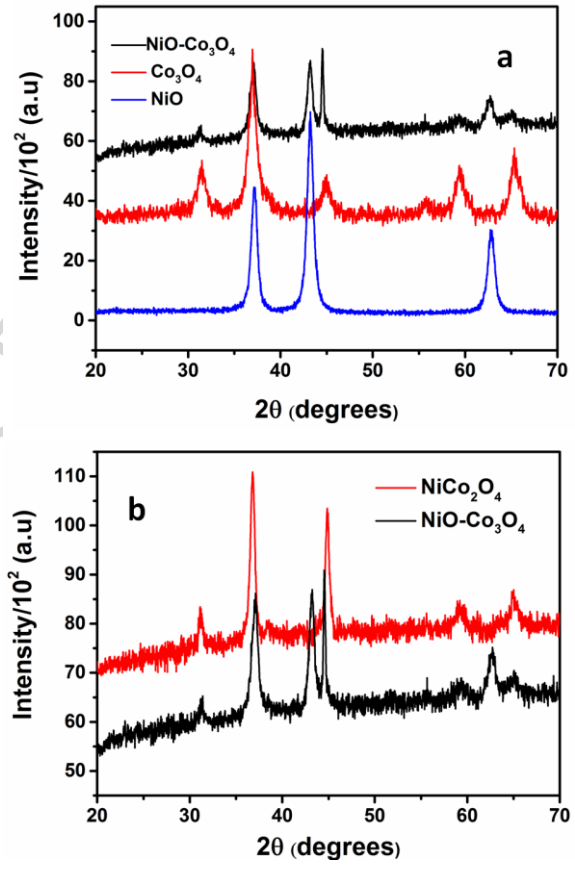

Figure 3. XRD pattern of NiO–Co_3O_4 (a) compared with its individual components; (b) compared with $NiCo_2O_4$

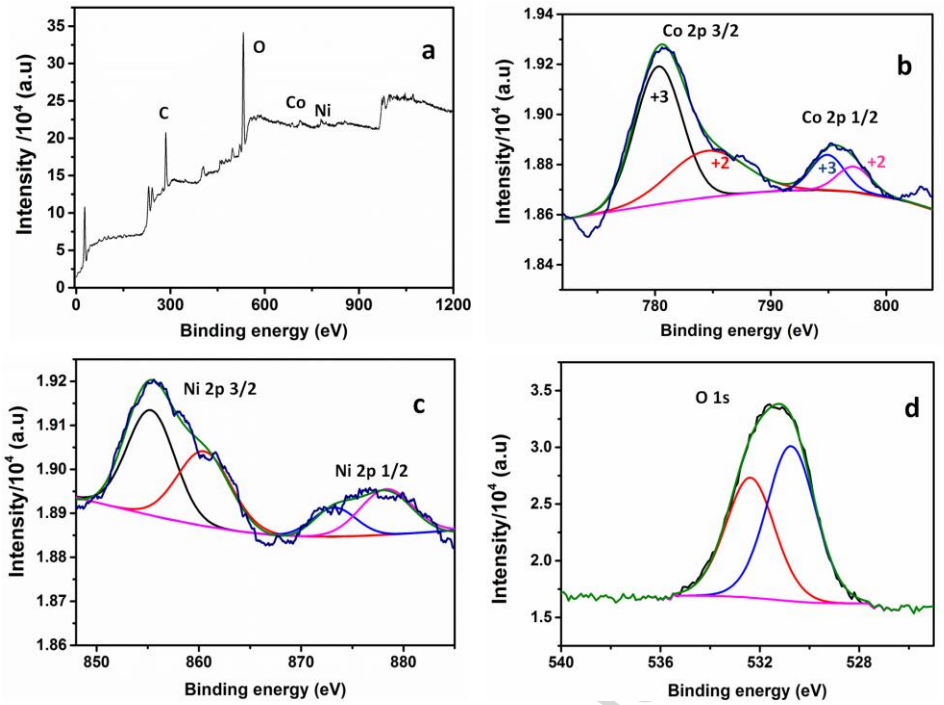

Figure 4. (a) XPS full survey scan spectrum of the NiO–Co_3O_4 nanobelts; (b)(c) (d) XPS spectra of Co 2p, Ni 2p and O 1s

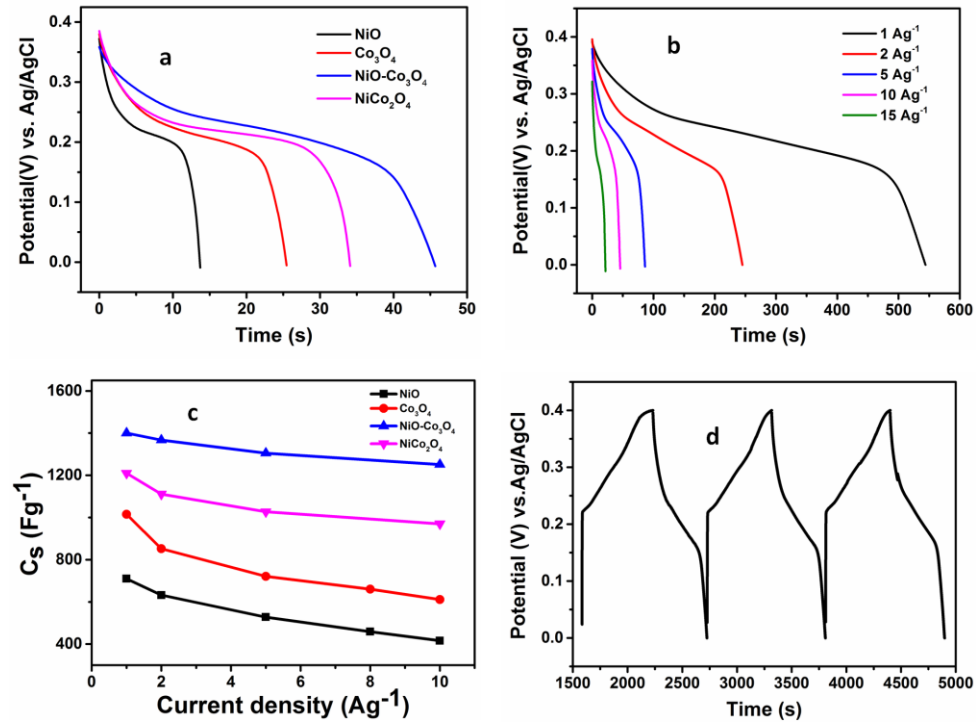

Figure 5. (a) Discharge curves of NiO, Co_3O_4, NiO–Co_3O_4 and $NiCo_2O_4$ at 10 A g^{-1}; (b) discharge profile of NiO–Co_3O_4 at different current densities; (c) variation of capacitance with current density of all the four materials; (d) CDC curves of NiO–Co_3O_4 at 1 A g^{-1}

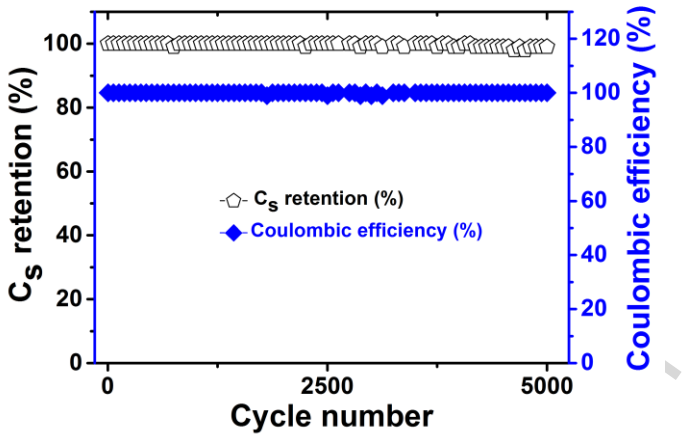

Figure 6. The cyclic stability of the NiO–Co_3O_4 nanobelts evaluated by galvanostatic charge-discharge testing at a current rating of 10 A g^{-1}

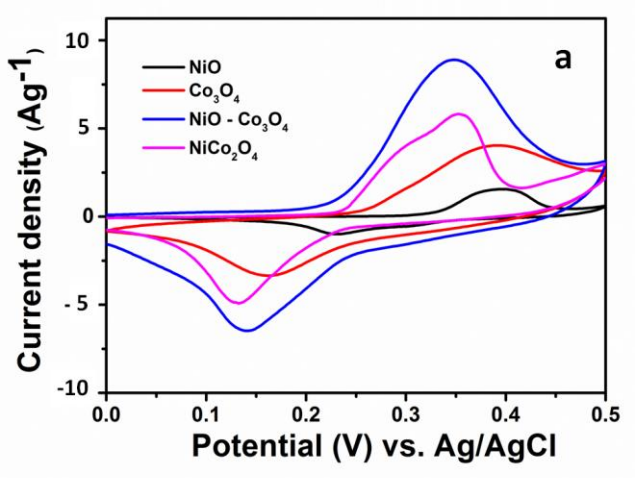

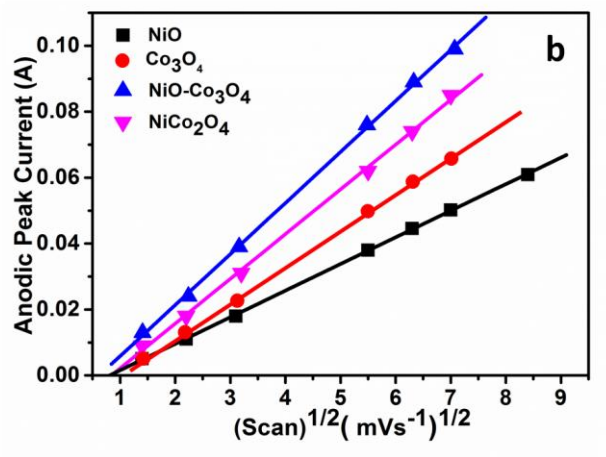

Figure 7. (a) Comparative CV curves of NiO, Co_3O_4, NiO–Co_3O_4 and $NiCo_2O_4$ at 5 mV s^{-1}; (b) linear variation of square root of scan rate ($v^{1/2}$) with voltammetric current (i) for all the materials under study

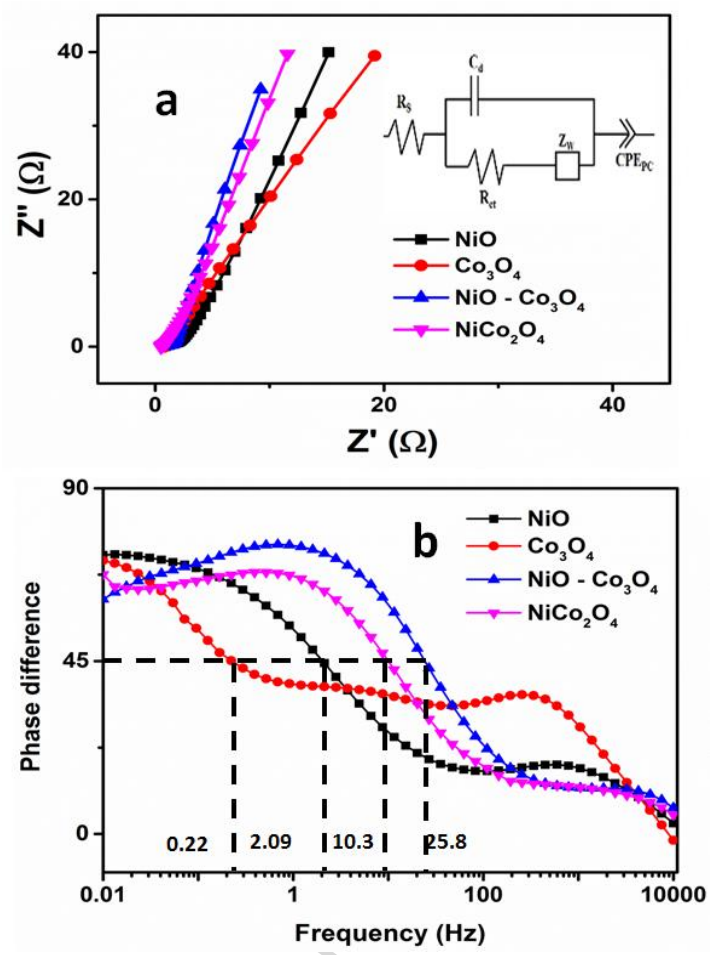

Figure 8. (a) EIS Nyquist spectra of NiO, Co_3O_4, NiO–Co_3O_4 and $NiCo_2O_4$ (inset– equivalent circuit for NiO–Co_3O_4); (b) variation of phase difference with frequency curve of all the materials under study

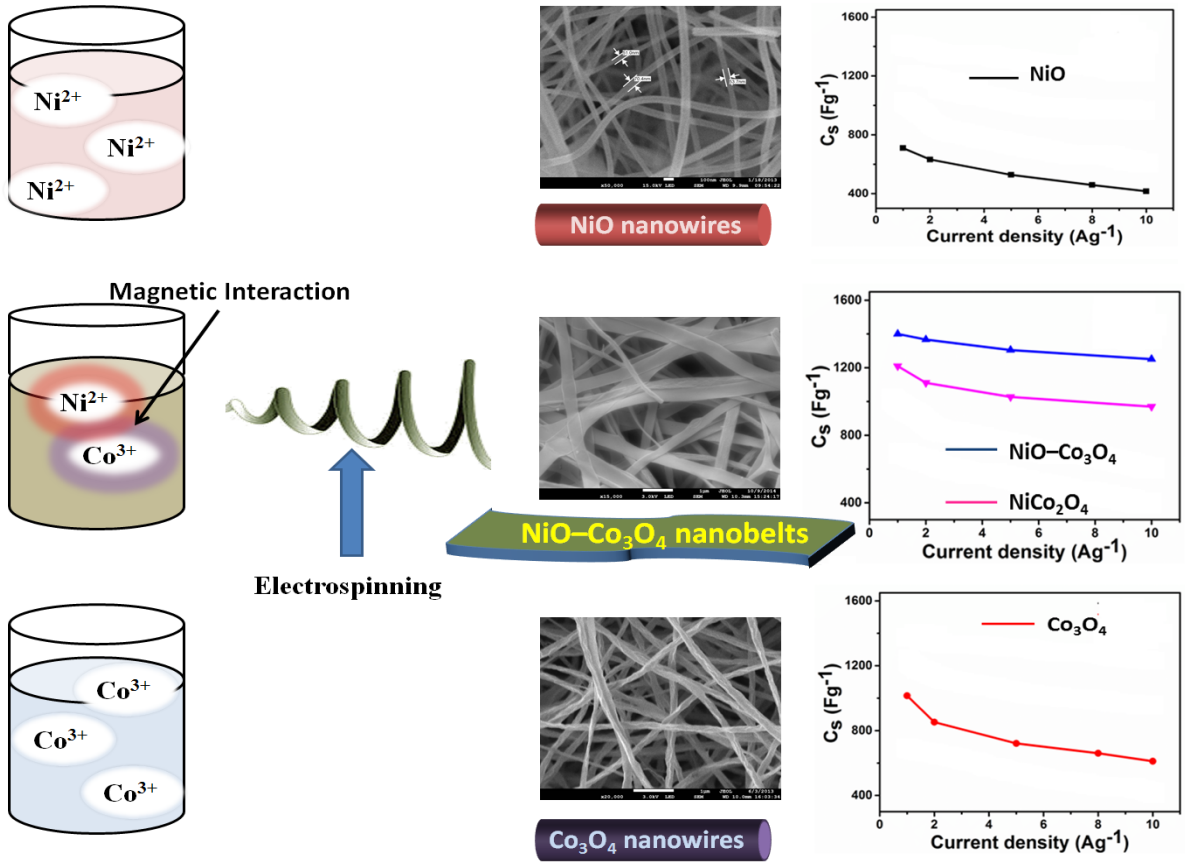

Graphical abstract

Highlights

- Continuous nanobelts of a material hybrid (HNBs) are prepared.
- Thickness of the HNBs is less than half of its pore diameter.
- Electrochemical properties of the HNBs are benchmarked with three other materials.
- HNBs showed superior charge storage properties.